New Phytologist

Single-cell multiome reveals root hair-specific responses to salt stress

Qing Liu[1]*, Jingmin Kang[2]*, Lin Du[2,3]*, Zhaokun Liu[4]*, Hao Liang[1], Kailai Wang[5], Haijiao He[1], Xiaonan Zhang[1], Qifan Wang[1], Yiguo Hong[1], Qi Cheng[1], Xin Liu[2], Wei Ma[1] and Jianjun Zhao[1]

[1]State Key Laboratory of North China Crop Improvement and Regulation, Key Laboratory of Vegetable Germplasm Innovation and Utilization of Hebei, Collaborative Innovation Center of Vegetable Industry in Hebei, Hebei International Joint Research and Development Center of Modern Agricultural Biotechnology, College of Horticulture, College of Life Sciences, Hebei Agricultural University, Baoding, 071000, China; [2]BGI Research, Beijing, 102601, China; [3]College of Life Sciences, University of Chinese Academy of Sciences, Beijing, 100049, China; [4]Suzhou Academy of Agricultural Sciences, Suzhou, Jiangsu, 215155, China; [5]Glbizzia Biosciences, Beijing, 102609, China

Authors for correspondence:
Jianjun Zhao
Email: jjz1971@aliyun.com

Wei Ma
Email: mawei0720@163.com

Xin Liu
Email: liuxin@genomics.cn

Received: *13 February 2025*
Accepted: *1 April 2025*

New Phytologist (2025) **246:** 2634–2651
doi: 10.1111/nph.70160

Key words: *BcIRT2*, non-heading Chinese cabbage, root hair, salt stress, single-nucleus multi-omics.

Summary

- Soil salinization, exacerbated by environmental deterioration and improper cultivation, is a major challenge for sustainable agriculture. The root is the primary organ in plants to perceive and respond to salt stress.
- Utilizing single-cell sequencing, we have created the first single-cell transcriptional and chromatin accessibility landscape for normal and salt-stressed root tips in non-heading Chinese cabbage (NHCC). Our study reveals that salt stress disrupts the normal differentiation of root hairs, leaving many in an undifferentiated state and preventing stress response gene expression. Inter-species analyses show that both salt and osmotic stresses inhibit root hair differentiation and elongation similarly, resulting in fewer, malfunctioning root hairs.
- We found that high salinity affects root hair iron transport. Salt stress-responsive genes, cell type-specific transcriptional regulatory networks, and trajectory curves are linked to iron transport. Specifically, the expression of *BcIRT2*, a metal transporter gene, is influenced by salt stress. Silencing *BcIRT2* causes chlorotic leaves and increases salt sensitivity, reducing iron content in NHCC roots.
- Our findings offer significant insights into plant salt stress responses and provide valuable information for breeding salt-tolerant NHCC and other crops.

Introduction

Immobile plants are naturally exposed to diverse biotic and abiotic stresses that often exert deleterious influences on their growth (Zhu, 2016; Zhang *et al.*, 2022). Climate changes, along with environmental pollution and irrational fertilization, have increased saline-alkalization and reduced global cultivatable lands. Saline-alkali soil impedes plant root growth and hinders leaf photosynthesis, leading to severe wilting, yellowing, or even mortality (Zhao *et al.*, 2020). Salt stress has emerged as one of the most devastating abiotic factors and prominent constraints that affect crop yield and quality in agriculture and horticulture worldwide (Yang & Guo, 2018).

Non-heading Chinese cabbage (NHCC, *Brassica campestris* (syn. *Brassica rapa*) ssp. *chinensis*) is an important leafy vegetable widely grown in many countries and regions around the world. NHCC produces sweet, juicy, and nutrient-rich leaves as the main edible organs (Li *et al.*, 2020). However, NHCC cultivation and production often face risks from high salinity. Generally, salt stress can cause delayed and uneven seed germination (Ren *et al.*, 2020). High salinity can also lead to high osmosis in the soil, which limits the absorption capacity and normal growth of the root system, resulting in leaf yellowing, plant wilting, and massive yield reduction (Wang *et al.*, 2022). However, few studies have examined the molecular mechanisms underlying salt stress in NHCC.

Traditional high-throughput sequencing often fails to detect the differences in gene expression among various cell types, disregarding the distinctive attributes of individual cells (Denyer *et al.*, 2019; Farmer *et al.*, 2021; Marand *et al.*, 2021; Zhang *et al.*, 2021; Mo & Jiao, 2022; Qu *et al.*, 2022; Li *et al.*, 2024). Moreover, numerous pivotal genes that govern the development of diverse cell types remain unidentified, and our understanding of the transcriptional regulatory network (TRN) response to salt stress in different cell types remains limited. Therefore, revealing dynamic, cell type-specific TRNs in NHCC under salt stress not

*These authors contributed equally to this work.

© 2025 The Author(s).
New Phytologist © 2025 New Phytologist Foundation.
This is an open access article under the terms of the Creative Commons Attribution-NonCommercial-NoDerivs License, which permits use and distribution in any medium, provided the original work is properly cited, the use is non-commercial and no modifications or adaptations are made.

only offers insights into how NHCC responds to salt stress at the single-cell level but also may contribute to developing new breeding strategies to enhance salt tolerance in NHCC and other crops (Shaw *et al.*, 2021; Sun *et al.*, 2022; Ding *et al.*, 2023; Ma *et al.*, 2023; Zhang *et al.*, 2023).

Root systems play a crucial role in absorbing water and mineral nutrients for plant development and growth (Libault *et al.*, 2010). They are the primary frontiers for perceiving soil salinity (Wong *et al.*, 2018; Wang *et al.*, 2020). In this study, we produced the single-nucleus multi-omics profiles for NHCC root tip cells under salt stress. We annotated the root cell types by employing Stereo-seq and RNA *in situ* hybridizations and characterized the NHCC single-cell landscapes of gene transcription and chromatin status. The single-cell gene regulatory networks (GRNs) enabled us to identify multiple stress-related cell type-specific regulators in NHCC roots. Moreover, cross-species single-cell transcriptome analyses revealed some conserved functions of root hair in responding to salt and osmotic stress.

Materials and Methods

Plant materials and growth conditions

For snRNA-seq and snATAC-seq, Non-heading Chinese cabbage (NHCC, *Brassica campestris* (syn. *Brassica rapa*) ssp. *chinensis*) plants were grown on ½ Murashige & Skoog (½MS) medium for 6 d (16 h : 8h, 23°C, light : dark, 250 μmol m^{-2} s^{-1}; control group), and a subset of plants was transferred to ½MS medium containing 150 mM NaCl for 12 h (stress group) (Wang *et al.*, 2022). Subsequently, 5-mm root tips of the control and stress groups were collected for extraction of root cell nuclei.

Nucleus isolation

The nuclear isolation procedure was partially modified according to the product information sheet of the CelLyticTM PN Isolation/Extraction Kit (Sigma). The root tips were chopped and added to precooled 1× NIBTA buffer (1× NIB, 1 mM dithiothreitol, 1× ProtectRNA™ RNase inhibitor, 1× cOmplete™, EDTA-free Protease Inhibitor Cocktail, and 0.3% Triton X-100). The mixture was shaken gently on ice for 5 min, followed by passing the mixture through a 40-μm filter and collecting the flow into a new 15-ml tube. The filtrate was centrifuged at 1260 ***g*** for 10 min, the supernatant was discarded, and the nuclei were resuspended in 4 ml 1× NIBTA buffer. The nuclei resuspension was added to a new 15-ml tube containing 75% Percoll solution. After centrifugation at 650 ***g*** for 30 min, the nuclei were located in the 1× NIBTA buffer and Percoll interface bands. Nuclei were gently collected into new 15-ml tubes, 10 ml of 1× NIBTA buffer was added, and centrifuged at 1260 ***g*** for 5 min. Finally, nuclei were washed twice in 1× NIBTA buffer and resuspended in PBS containing 0.04% BSA to a final concentration of 2000 nuclei μl^{-1} (for snRNA-seq), or in PBS containing 1% BSA to a final concentration of 6000 nuclei μl^{-1} (for snATAC-seq).

Single-nucleus RNA library construction

The snRNA-seq libraries were prepared as previously described (Liu *et al.*, 2019) with DNBelab C Series High-throughput Single-Cell RNA Library Preparation Kit (940-000047-00; MGI, Qingdao, China). Individual nuclei were co-encapsulated with barcoded beads into droplets. These barcodes specifically labeled the poly-A-tailed RNA released from the nuclei, providing a crucial basis for the subsequent precise identification of individual nuclei. Subsequently, the droplets were subjected to emulsion breaking to release their contents, followed by the collection of the barcoded beads. Next, reverse transcription was performed to convert the poly-A-tailed RNA into cDNA, which was then amplified to generate a sufficient quantity of barcoded libraries for sequencing analysis. The resulting libraries were sequenced using MGI 2000 and DNBSEQ T7. The read length was as follows: Read 1 was 30 bp, including 10 bp cell barcode 1, 10 bp cell barcode 2, and 10 bp unique molecular identifiers (UMI); Read 2 was 100 bp for transcript and 10 bp for sample index.

Single-nucleus ATAC library construction

The snATAC-seq libraries were prepared as previously described (Lei *et al.*, 2022) with DNBelab C Series Single-Cell ATAC Library Prep Set (1000021878; MGI). First, the nuclei were transposed using the Tn5 transposase. After transposition, droplet encapsulation was performed to isolate individual nuclei along with barcoded beads. Pre-amplification was then carried out to enrich the DNA fragments from the open chromatin regions that had been tagged by transposition. This was followed by emulsion breaking to release the beads, and the captured beads were collected. Finally, DNA amplification and purification were performed to generate the single-nucleus ATAC library, which was ready for sequencing. The resulting libraries were sequenced using MGI 2000 and DNBSEQ T7. The read length was as follows: Read 1 was 70 bp, including 10 bp for cell barcode 1, 10 bp for cell barcode 2, and 50 bp for open chromatin; Read 2 was 50 bp for open chromatin and 10 bp for sample indexing.

Spatial transcriptomics library construction

Stereo-seq uses standard DNA nanoball sequencing chips, with spots *c.* 220 nm in diameter and a center-to-center distance of 500 nm (Martin & Wang, 2011; Bawa *et al.*, 2024). Stereo-seq data of NHCC root tips allows us to explore cell subtypes and their specific gene profiles in detail. Stereo-seq (Chen *et al.*, 2022) was used to construct spatial transcriptomics libraries. The root tip (control group) was embedded in OCT and sectioned into 10-μm slices. These slices were then adhered to Stereo-seq chips. The chips containing tissue sections were incubated at 37°C for 3 min. Methanol fixation, permeabilization, reverse transcription, tissue removal, cDNA release, and library preparation were next performed using previously described methods (Xia *et al.*, 2022). Finally, DIPSEQ T10 was used for sequencing.

© 2025 The Author(s).
New Phytologist © 2025 New Phytologist Foundation.

Histochemical staining

The 6-d-old root tips (5 mm) of NHCC culturing in normal conditions were excised and fixed in a solution containing 3.7% formaldehyde, 5% acetic acid, and 50% ethanol. The fixed tissue was then dehydrated using an ethanol series. Subsequently, the samples were embedded in paraffin, sectioned into slices with a thickness of 8 mm, and mounted onto microscope slides (Fisher Scientific, Waltham, MA, USA). After deparaffinization and hydration to distilled water, the sections were immersed in the spirit blue solution (with 0.01% spirit blue) for 60 s before being rinsed with distilled water. After coloration, rapid dehydration through an ethanol series was performed. Finally, the samples were observed under a light microscope (Leica DM6 B, Wetzlar, Hesse (Hessen), Germany).

Perls staining was performed as reported previously to measure the iron content in NHCC root hairs and leaves (Roschzttardtz *et al.*, 2009; Vargas & Roschzttardtz, 2023). For the leaves, we first performed Prussian blue staining; after this step, DAB (Diaminobenzidine) intensification was used to visualize easily.

RNA *in situ* hybridization

The specific regions of marker genes were cloned into the pGEM-TEasy (Promega) vector, followed by *in vitro* transcription and labeling using the Digoxigenin RNA labeling kit (Roche). The hybridization and immunological detection procedures were conducted as previously described (Zhao *et al.*, 2009; Liang *et al.*, 2015), while microscopy was performed in bright-field mode utilizing Leica DM6 B. The primers used in these analyses are detailed in Supporting Information Table S1.

Virus-induced gene silencing

BcIRT2 was silenced via virus-induced gene silencing (VIGS) in NHCC plants as previously described (Yu *et al.*, 2018).

The 40-bp interfering fragment (5′-CTGATCCACAAC TTCTACGGTACCGTGTCATTGCTATGGTACCATAGC AATGACACGGTACCGTAGAAGTTGTGGATCAG-3′) and its antisense sequence of *BcLRT2* was cloned into the pTY vector to produce pTY/BcLRT2. pTY/BcLRT2 plasmid DNA was bombarded onto young leaves of NHCC 'Xiangqingcai' seedlings using a Biolistic PDS-1000/He (Bio-Rad). The empty pTY vector was used as a control. At 10 d post bombardment, new leaves and roots were collected, and *BcIRT2* expression was examined using RT-qPCR (real-time quantitative polymerase chain reaction).

Real-time quantitative PCR

Seedlings transformed by gene gun culturing in normal conditions were collected for total RNA extraction. Total RNA was extracted by using an RNeasy Plant Mini Kit (Qiagen). Then, these samples were analyzed by RT-qPCR using SYBR Green Supermix (TOYOBO) on an Applied Biosystems 7500 Fast Real-Time PCR system. The primers used in these analyses are detailed in Table S2.

snRNA-seq data preprocessing

C4 DNBelab_C_Series_HT_scRNA-analysis-software (v.2.0) (Liu *et al.*, 2019) was utilized for the processing of raw files. This encompassed various tasks such as decomposing FASTQ files, extracting barcodes, counting UMIs, filtering, and aligning reads to both the *Brassica* reference genome (CAAS_Brap_v.3.01; Zhang *et al.*, 2018) and its mitochondrial genome. The result was the creation of a matrix sample that encompassed normalized gene counts and nucleus numbers. Following this, the obtained matrix sample underwent quality control and downstream analysis in the R package SEURAT (v.4.3) (Hao *et al.*, 2021). Default parameters were applied unless stated otherwise. Notably, cell filtering in this study was based on the criterion of gene counts surpassing the mean ± 2 times the SD. This led to the exclusion of unpaired doublets, apoptotic nuclei, other unpaired or low-quality nuclei, and potential multiple captures. In the phase of filtering low-quality single cells, those with a gene count < 200 or UMI < 5500 were excluded. Ultimately, the downstream analysis comprised 30 771 nuclei, with a minimum gene count of 1192.

snATAC-seq data preprocessing

The raw reads underwent processing using PISA (v.0.7) (Shi *et al.*, 2022) and were subsequently aligned to the genome reference (CAAS_Brap_v.3.01; Zhang *et al.*, 2018) using BWA (v.0.7.17-r1188) (Li & Durbin, 2010) to generate BAM files. Subsequently, bap2 was employed to generate fragment files for each snATAC-seq library (Lareau *et al.*, 2019). Only the sequencing reads aligned to the nuclear genome were retained for further analysis. We used D2C (v.1.3.8) to assign sequencing barcodes for cell barcoding. Based on the alignment results for each nucleus, peak calling was performed using MACS2 (v.2.2.7.1) with the parameters '-B -q 0.001 –nomodel' (Zhang *et al.*, 2008). Subsequent analysis utilized the ARCHR (v.1.0.1) package (Granja *et al.*, 2021). Only nuclei meeting the following criteria were retained for further analysis: transcription start site enrichment score of at least 1.2, unique nuclear fragment counts between 2000 and 50 000, and a fraction of reads in peaks (FRiP) > 0.2.

Cell clustering and annotation for snRNA-seq data

The downstream analysis of snRNA-seq data predominantly relied on the SEURAT software package, as mentioned earlier (v.4.2) (Hao *et al.*, 2021). Initially, to address batch effects, canonical correlation analysis (CCA) was employed to evaluate the correlation among single-cell data from diverse samples (Zhang *et al.*, 2019). This involved three functions from the Seurat package (SelectIntegrationFeatures, FindIntegrationAnchors, and IntegrateData), with default parameters facilitating the integration of datasets from distinct samples. Subsequently, the 'NormalizeData' function was applied, utilizing the LogNormalize method with a scaling factor of 10 000, and the log1p function for standardizing the quality-controlled data. Following the identification of variable genes via the 'FindVariableGenes' function

© 2025 The Author(s).
New Phytologist © 2025 New Phytologist Foundation.

(using the vst method and selecting the top 2000 features), the data underwent scaling using the ScaleData function. Principal component analysis (PCA) was executed using the 'RunPCA' function in Seurat, selecting 30 principal components, while graph-based clustering utilized the 'FindClusters' function, employing the Leiden algorithm (Traag *et al.*, 2019) with a resolution of 0.4. Finally, the data were visualized through the application of the nonlinear dimensionality reduction algorithm (RunUMAP function). Additionally, we manually annotated the 18 clusters obtained using known cell type-specific marker genes and differentially expressed genes (DEGs).

Quality control of Stereo-seq data

The expression data of NHCC root tip was extracted from the complete Stereo-seq (Chen *et al.*, 2022) dataset and was transformed into bin 30 Stereo-seq data (corresponding to cell-sized pseudo-spots measuring 15 μm square). The quality control process was conducted using the Scanpy-1.9.1 package within Python (v.3.9.15) software (Wolf *et al.*, 2018). To eliminate cells of low quality, we analyzed the distribution of expression levels and gene counts in each bin. We found that the distribution of total UMI count and total gene count per cell of Stereo-seq data showed a unimodal distribution, and therefore, we did not filter out the cells in bin 30. Moreover, cells containing a high proportion (> 5%) of mitochondrial genes were also removed due to their low quality. After filtering, the remaining 786 single cells with 16 028 genes were included in downstream analyses.

Clustering and DEG analysis of Stereo-seq data

Clustering analysis and the identification of DEGs were conducted on the NHCC root tip Stereo-seq dataset using the Scanpy package in Python. Initially, we normalized the total count in the data matrix to 10 000 reads per cell, making counts comparable across cells. Afterward, the dimensionality of the data was reduced through PCA, revealing the main sources of variation and improving data denoising. Subsequently, we generated the neighborhood graph of cells using the top 30 principal components and embedded it in two dimensions using uniform manifold approximation and projection (UMAP). The Leiden graph-clustering effectively grouped cells based on their neighborhood relationships within the graph (Traag *et al.*, 2019). Furthermore, a ranking of DEGs within each cluster was computed using the *t*-test. The default parameters were employed for the *t*-test, and the default parameters were used ($P < 0.05$).

Correlation analysis between snRNA-seq and snATAC-seq

The integration of snRNA-Seq and snATAC-Seq data was conducted using the Seurat package (v.4.3). In this step, snRNA-Seq data served as the reference dataset, and a classifier was trained to automatically assign cell types to each snATAC-Seq cell. Initially, to pinpoint anchors between snRNA-Seq and snATAC-Seq experimental data, the 'GeneActivity' function in the ArchR package was employed (Granja *et al.*, 2021). This function quantifies ATAC-seq counts in the 2 kb upstream region and within the gene body, generating a transcriptional activity score for each gene. The gene activity scores from snATAC-seq data, along with quantified gene expression from snRNA-seq, were employed as inputs for correlation analysis. This facilitated the quantification of all genes identified as highly variable in the snRNA-seq dataset. Following the identification of anchor points, annotation from the snRNA-seq dataset was transferred to snATAC-seq cells using the 'TransferData' function and 'AddMetaData' function. The annotations were stored in seurat_annotations and served as input for the refdata parameter. This process yielded predictions and confidence scores for each ATAC-seq cell. Additionally, the uncertainty associated with predicted annotations was quantified using 'prediction.score.max'. Cells correctly annotated typically exhibited a high prediction score (> 90%), while cells with incorrect annotations had lower prediction scores.

To evaluate the correspondence between snRNA-seq and snATAC-seq annotations, we calculated the Jaccard index for each pair of cell types identified in both datasets. First, cell types were annotated based on clustering results from the RNA-seq data and transferred to the ATAC-seq data using label transfer algorithms. For each pair of RNA-seq and ATAC-seq cell types, we defined the Jaccard index as the size of the intersection divided by the size of the union of the annotated cells. This index quantifies the overlap between the two datasets, where an index of 1 indicates perfect correspondence and an index of 0 indicates no overlap.

Identification of DEGs

We utilized the 'FindAllMarkers' function in Seurat, implementing the Wilcoxon rank-sum test and employing Bonferroni correction to adjust *P*-values for multiple testing. This function was instrumental in computing cluster-enriched genes by comparing each cluster to the union of all other clusters. A threshold was set for differences between the two cell groups, ensuring a minimum fold change of 1.3 ($\log_2$ (fold change threshold) = 0.25), and statistical significance was established at an adjusted *P*-value < 0.05. This approach allowed us to discern genes that were specifically enriched within individual clusters, shedding light on distinctive molecular characteristics associated with each cell group.

For stress-related differentially expressed genes identification, we use the method in Seurat followed by a Wilcoxon rank-sum test. The criteria for identifying differentially expressed genes were $|\log_2$ fold change$| > 0.25$ and adjusted *P*-value < 0.05.

Enrichment analysis

We performed comprehensive Gene Ontology (GO) and Kyoto Encyclopedia of Genes and Genomes (KEGG) pathway analyses on the differentially expressed genes to uncover their potential functional enrichments and biological signal transductions. The GO analysis spanned biological process, cellular component, and molecular function categories, while the KEGG pathway analysis covered metabolism, environmental information processing,

© 2025 The Author(s).
New Phytologist © 2025 New Phytologist Foundation.

organismal systems, genetic information processing, and cellular processes. These analyses were executed using the 'clusterProfiler' package in R. Terms with adjusted *P*-value below 0.05 were recognized as significantly enriched, providing valuable insights into the biological processes and pathways associated with the identified genes.

Pseudo-time analysis

The *Arabidopsis* root hair single-cell data used in this study were generated from our previous work (Liu *et al.*, 2024). We conducted an analysis of the differentiation trajectory in root cells using the R package Monocle2 (v.2.0) (Qiu *et al.*, 2017). Initially, the raw counts were converted into the CellDataSet format through the importCDS function (object, import_all = FALSE). Following this, the 'estimateSizeFactors' and estimateDispersions functions were applied to pre-calculate critical parameters associated with the data. The 'differenceGeneTest' function was subsequently employed to identify potential ordering genes (qval < 1e-4), supplying essential information for arranging cells along the pseudo-time trajectory. Differentially expressed genes specifically marked for ordering were then pinpointed using the 'setOrderingFilter' function. A dimensionality reduction clustering analysis was carried out using the 'reduceDimension' function (max_components = 2, reduction_method = 'DDRTree'), and trajectory inference was conducted with default parameters utilizing the 'orderCells' function. This comprehensive approach allowed for a detailed exploration of the differentiation dynamics within the root cell population. The R package ClusterGVis was used for visualization of these genes' expression.

TRN analysis

The pySCENIC tool (v.0.11.2) played a pivotal role in our transcription factor (TF) analysis (Kumar *et al.*, 2021). This sophisticated software was harnessed to infer TFs within single-cell transcriptomic data, delineate their target genes, and construct comprehensive regulatory networks. This not only allowed for an intuitive exploration of gene expression regulatory relationships but also facilitated the identification of distinct cellular states. The initial step involved the conversion of the fully processed Seurat object, complete with cell type annotations, into a loom file. Subsequently, this loom file served as the input for the SCENIC workflow (Aibar *et al.*, 2017). Through the application of Gene Regulatory Network Boosting (GRNBoost) analysis, we discerned potential target genes for each TF, culminating in the formation of a co-expression network. Following this, R*cis*Target was employed to conduct *cis*-regulatory motif analysis for each co-expression module. This meticulous process enabled the retention of direct targets with accurately enriched upstream regulators. In the subsequent phase, AUCell was enlisted to score the target genes of regulatory factors, effectively calculating the activity of regulatory elements. This scoring system, in turn, facilitated the classification of cells based on their regulatory activity, providing a nuanced understanding of cellular dynamics. The R package scPlant was used for visualization of TF-related gene expression.

Results

Combined snRNA-seq, snATAC-seq, and Stereo-seq generate a single-cell transcriptome atlas of the NHCC root

We conducted both snRNA-seq and snATAC-seq on nuclei isolated from 5-mm root tips under 150 mM NaCl salt stress for 12 h (salt stress) and normal growth conditions (control) (Fig. 1a), respectively; two biological replicates (seedings cultured in two independent experiments) were performed for each sample. Following quality control filtering, 30 771 nuclei were identified, with an average of 3163 genes detected per nucleus for snRNA-seq (Table S3). In addition, a total of 24 671 nuclei were retained for snATAC-seq, yielding an average of 9431 fragments per nucleus. We performed UMAP on snRNA-seq data and identified eight distinct cell types (Fig. 1b–d). Our single-cell transcriptome data showed high concordance between biological and technical replicates (Fig. S1a,b). While root cell type marker genes of *Brassica* are largely unknown, NHCC exhibits high homology with *Arabidopsis thaliana* within the cruciferous family. Consequently, we utilized well-studied marker genes from *A. thaliana* to annotate NHCC data in our initial analysis (Sun *et al.*, 2022) (Figs 1e, S2; Table S4). We found that more than 20 orthologs of known marker genes for diverse *Arabidopsis* cell types showed cell type-specific expression patterns in NHCC. These cell types, including root hair, endodermis, epidermis, dividing cells, stele, and root cap, were annotated using orthologous markers. On the other hand, the development of some cell types in root tips differed between *Arabidopsis* and NHCC. For instance, 3–4 layers of cortex cells were developed in NHCC (Fig. S3), whereas only one layer formed in *Arabidopsis* (Zhang *et al.*, 2019; Shahan *et al.*, 2022). We found that the orthologs of known marker genes for the cortex of *Arabidopsis* did not possess cell type-specific expression in NHCC (Wendrich *et al.*, 2020; Farmer *et al.*, 2021; Shahan *et al.*, 2022) (Fig. S4). Consequently, cell types such as the cortex and initial in the NHCC root tips, could not be annotated using *Arabidopsis* orthologous genes.

To address this and verify the accuracy of homologous gene annotation, we used Stereo-seq to capture the spatial expression of genes in NHCC root tips grown under normal conditions (Fig. S5). We classified the Stereo-seq data into five clusters based on their spatial information and histological features, including epidermis, cortex, stele, and initial (Fig. 1f), and identified potential marker genes. For example, we uncovered that *LOC103858637* was specifically expressed in the cortex and a small number of initial cells, *LOC103858639* was specifically expressed in cortex cells, while *LOC103249170* and *LOC103860386* were specific to stele cells (Fig. 1g). We then mapped the cell-specific marker genes identified in the Stereo-seq onto the single-cell data and clustered genes in association with the cell-specific marker genes (Fig. 1h). In addition, we performed RNA *in situ* hybridization to validate the expression of cluster-specific marker genes in root tips (Fig. S6). We defined novel cell type-specific marker genes, constructed an anatomical diagram illustrating the annotated cell clusters and their respective spatial distributions within the root, and successfully

© 2025 The Author(s).
New Phytologist © 2025 New Phytologist Foundation.

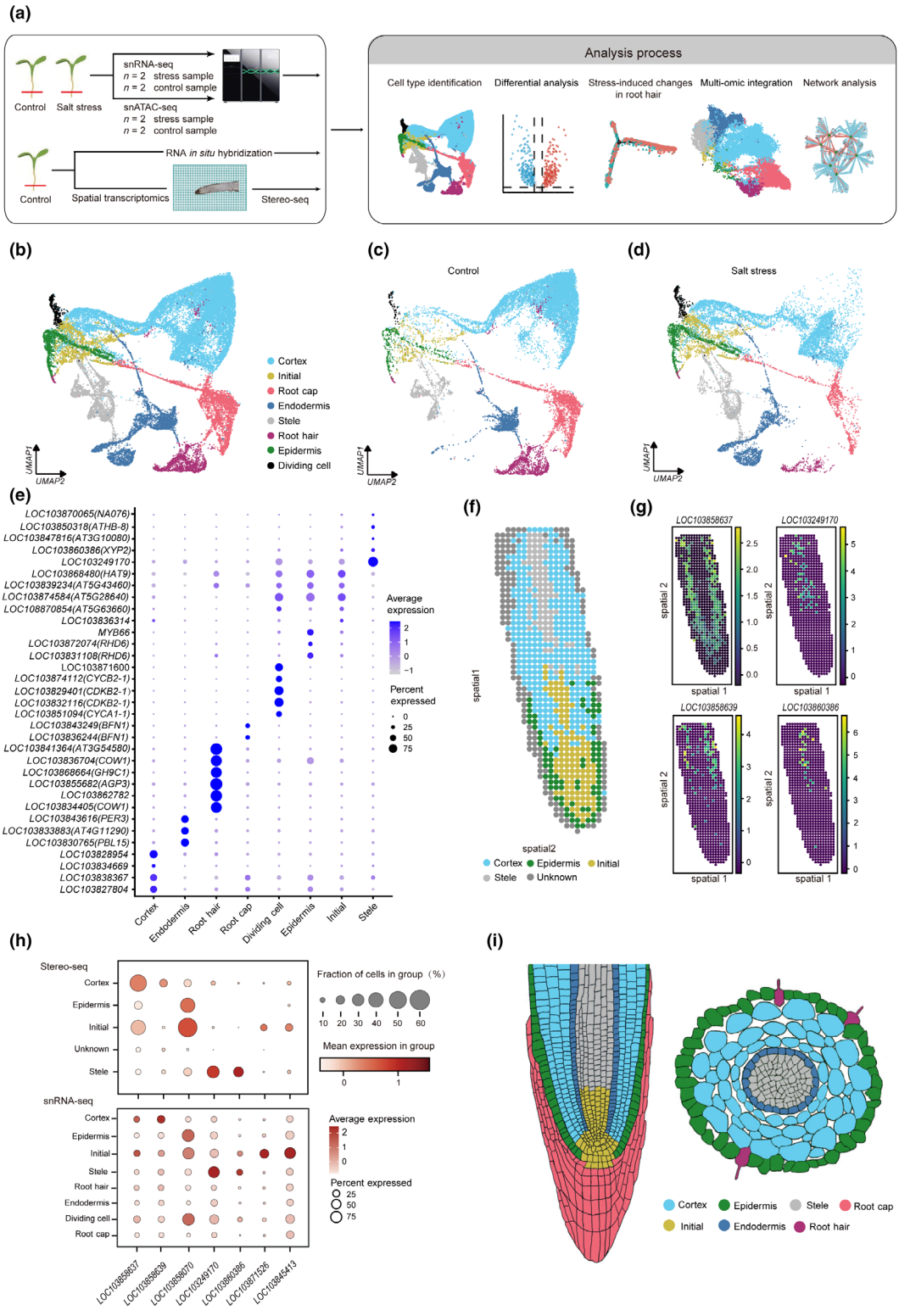

Fig. 1 Combined single-nucleus and spatial transcriptomes generate a single-cell transcriptome atlas of the non-heading Chinese cabbage (NHCC) root. (a) Overview of NHCC root tip single-cell multi-omics workflow. (b–d) Uniform manifold approximation and projection (UMAP) visualization of 30 771 single cells derived from NHCC root tips and annotated by RNA expression. (e) Expression of marker genes in each cell type. Dot size indicates the percentage of cells expressing the gene (% expressed). Dot colors represent the proportional amount of expression of each gene in each cell type, with deeper colors indicating higher expression levels. (f) Spatial distribution of different cell types. (g) Spatial distribution of cortex/stele marker genes. (h) Spatial expression patterns of transcriptome-identified cell type-specific genes in Stereo-seq (upper panel) and snRNA-seq (lower panel). (i) Schematic diagram of NHCC root tip.

© 2025 The Author(s).
New Phytologist © 2025 New Phytologist Foundation.

generated the first single-cell transcriptome atlas encompassing all major cell types in NHCC root tips (Fig. 1i).

Cell type-specific responses to salt stress in NHCC

Using the transcriptome atlases created from normal vs salt-stressed NHCC root tips, we analyzed DEGs across eight cell types (Fig. 2a,b). We observed variations in the number of DEGs among different cell types; for example, compared to other cell types, the cortex, root hair, stele, and endodermis contained more cell-specific DEGs in both the up-regulated and downregulated DEGs (Fig. 2a,b). Notably, most of the DEGs were cell-specific, indicating that different cell types had unique responses to salt stress. These results suggested the importance of conducting transcriptomic analysis at single-cell levels. To provide insights into the molecular functions in each cell type, we performed GO enrichment analysis of the stress up-regulated genes in each cluster (Fig. 2c; Table S5). We observed that genes associated with response to toxic substances and wounding were enriched in the endodermis, epidermis, and root cap, suggesting that these cell types could respond and adapt to salt stress more rapidly. Additionally, we observed significant enrichments of 'ribosome-related' terms in the cortex, root hair, and stele. Ribosomes are the cellular machinery for protein synthesis, and the upregulation of ribosome-related genes suggested that the general protein translation capacity was enhanced in these cells under salt stress (Fig. 2c). Under salt stress, the expression of genes related to root development was inhibited in initial cells, genes associated with responses to abiotic and environmental stimuli were reduced in root hair, and genes related to catabolic process were downregulated in cortex, stele, and endodermis cells (Fig. 2d).

To explore the value of our snRNA-seq data in uncovering specific salt stress response mechanisms, we analyzed the cell type-specific expression changes for genes known to be associated with salt stress. Abscisic acid (ABA) functions as a vital stress-responsive hormone, playing an indispensable role in salt stress defense (Yu *et al.*, 2020). To address these, we generated expression plots for ABA biosynthetic and transport genes (Fig. 2e; Table S6). Stele played a central role in plant hormone signaling (Ramachandran *et al.*, 2021; Waadt *et al.*, 2022). Consistent with this, we discovered that *ZEP*, *AA03*, *ABCG25*, *NCED5*, *NCED3*, *ABI3*, and *ABA3* were especially expressed in the stele (Fig. 2e), and most of these genes were induced by salt stress. Similar to ABA, salt stress can induce ethylene accumulation in plants (Zhang *et al.*, 2016; Yu *et al.*, 2020). Accordingly, ethylene biosynthesis genes were specifically expressed in the cortex, root cap, stele, and endodermis. For instance, salt stress activated the expression of *ACS6*, *ACS2*, *ACO4*, and *ACO5* in the stele. However, their expression in the root cap, cortex, and endodermis was inhibited by salt stress. Salicylic acid (SA) promotes photosynthesis in plants under salt stress and also plays an important role in plant salt tolerance (Ahanger *et al.*, 2019; Filgueiras *et al.*, 2019). There was no significant cell type-specific expression of genes involved in SA biosynthesis, and these genes had different expression patterns before and after salt stress (Fig. 2e). These results indicated that phytohormones, such as ABA, had spatiotemporal specificity in regulating plant responses to salt stress.

Given that the different cell types under salt stress had different response patterns (Dinneny *et al.*, 2008; Geng *et al.*, 2013) (Fig. 2c,d), we collected homologs of salt stress-related genes that have been well-studied in *Arabidopsis* and investigated their expression patterns across different cell types (Fig. 2f; Table S7). There had been several genome duplication and loss events during the evolution of *Brassica rapa* (Cai *et al.*, 2021), so we examined the expression of more than one homolog. Notably, these genes were cell type specifically induced in the stress group. Several of these genes, including *WRKY46*, *MAPKKK18*, *OSCA1.3*, and *ABI2*, were predominantly induced in the root cap after salt stress. Previous studies showed that high expression of *HARDY* improves salt stress tolerance in rice and *Arabidopsis* (Karaba *et al.*, 2007). In our study, the expression levels of the two homologs of *HARDY* were induced in different NHCC cell types. *HARDY-1* was highly induced in initial cells after salt stress; *HARDY-2* had a higher expression in root cap and stele cells and was further induced in root cap but suppressed in stele. Plants used calcium-dependent protein kinases of the salt overly sensitive (SOS) pathway to mediate salt stress signaling and sodium tolerance (Zhu, 2016). Our single-cell data indicated that *SOS1* was specifically expressed in the cortex, with no significant change in expression level before and after stress (Fig. 2f). *AFP4/TMAC2*, an important negative regulator of ABA and salt stress response (Huang & Wu, 2007), was expressed in dividing cells, as well as in cortex, root hair, and stele cells of NHCC; its expression was repressed under salt stress.

Salt stress shifted the physiological state of root hair

Salt stress could induce widespread responses in gene expression, metabolism, and physiological traits in plants. Indeed, we observed that salt stress exerted a significant impact on the proportion of various cell types in the root tip, and the number of root hair cells dramatically decreased under salt stress (Figs 3a, S7a; Table S8). In the root tip, both the length and the density of root hairs were significantly inhibited by salt stress (Figs 3b, S7b–c), consistent with the decrement of root hair cells in single-nucleus transcriptomic sequencing data (Figs 3a, S7a). Moreover, root hair density and length were reduced in the maturation zone under salt stress, while root hair density and length were increased in the meristem under salt stress (Fig. S7d,e). Root hairs are specialized structures that develop from the outermost epidermal layer, and salt treatment can alter the spatial distribution of hairless cells (N cells) and hairy cells (H cells) in *Arabidopsis* (Wang *et al.*, 2008). In the root tips of NHCC, the outermost epidermal layer consisted of two hairless cells (adjacent to one cortex; red arrow) and one hairy cell (adjacent to two cortex; black arrow) arranged alternately, similar to *Arabidopsis*. After 12 h of treatment with 150 mM NaCl, the spatial arrangement of hairless and hairy cells did not change significantly (Fig. S7f), which differed from *Arabidopsis* (Wang *et al.*, 2008). Additionally, most hairy cells did not develop significant bulges in the stress group (Fig. S7f).

© 2025 The Author(s).
New Phytologist © 2025 New Phytologist Foundation.

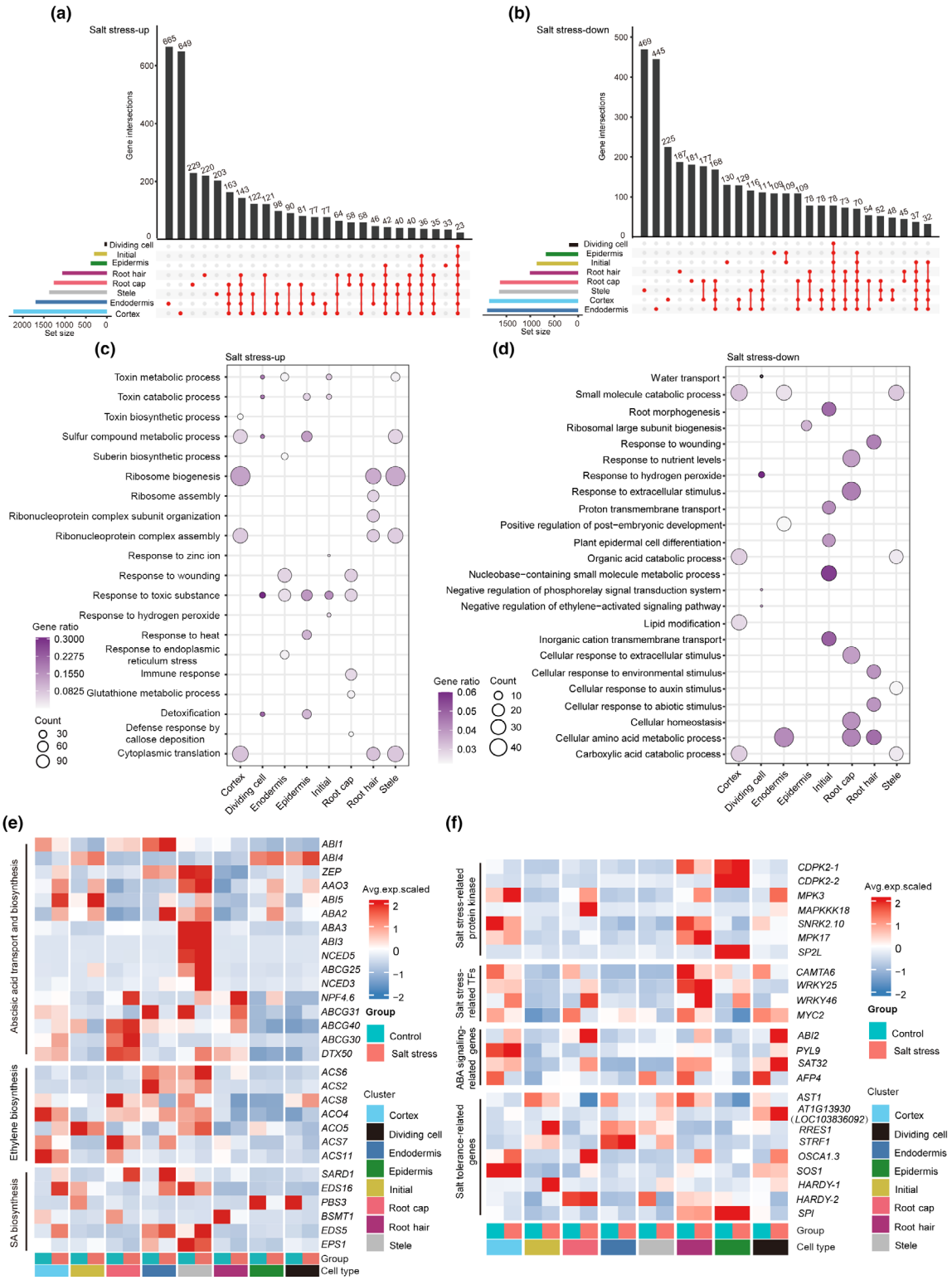

Fig. 2 Cell type-specific responses to salt stress. (a, b) Upset plot of stress upregulated (a) and downregulated (b) expressed genes among different cell types. (c, d) Dot plots of Gene Ontology (GO) enrichment analysis of stress upregulated (c) and downregulated (d) genes in each cluster. (e) Heatmaps showing relative expression of the genes related to ethylene biosynthesis, abscisic acid (ABA) transport and biosynthesis, and SA biosynthesis in each annotated cell type. Gene expression levels were represented by aggregated unique molecular identifiers (UMI) counts in all the cells belonging to the same cell type and in the same treatment. (f) Heatmaps showing relative expression of well-known stress-related genes from *Arabidopsis thaliana* homologs in each annotated cell type and with or without salt stress. Gene expression levels were represented by aggregated UMI counts in all the cells belonging to the same cell type and in the same treatment. SA, salicylic acid; TF, transcription factor.

© 2025 The Author(s).
New Phytologist © 2025 New Phytologist Foundation.

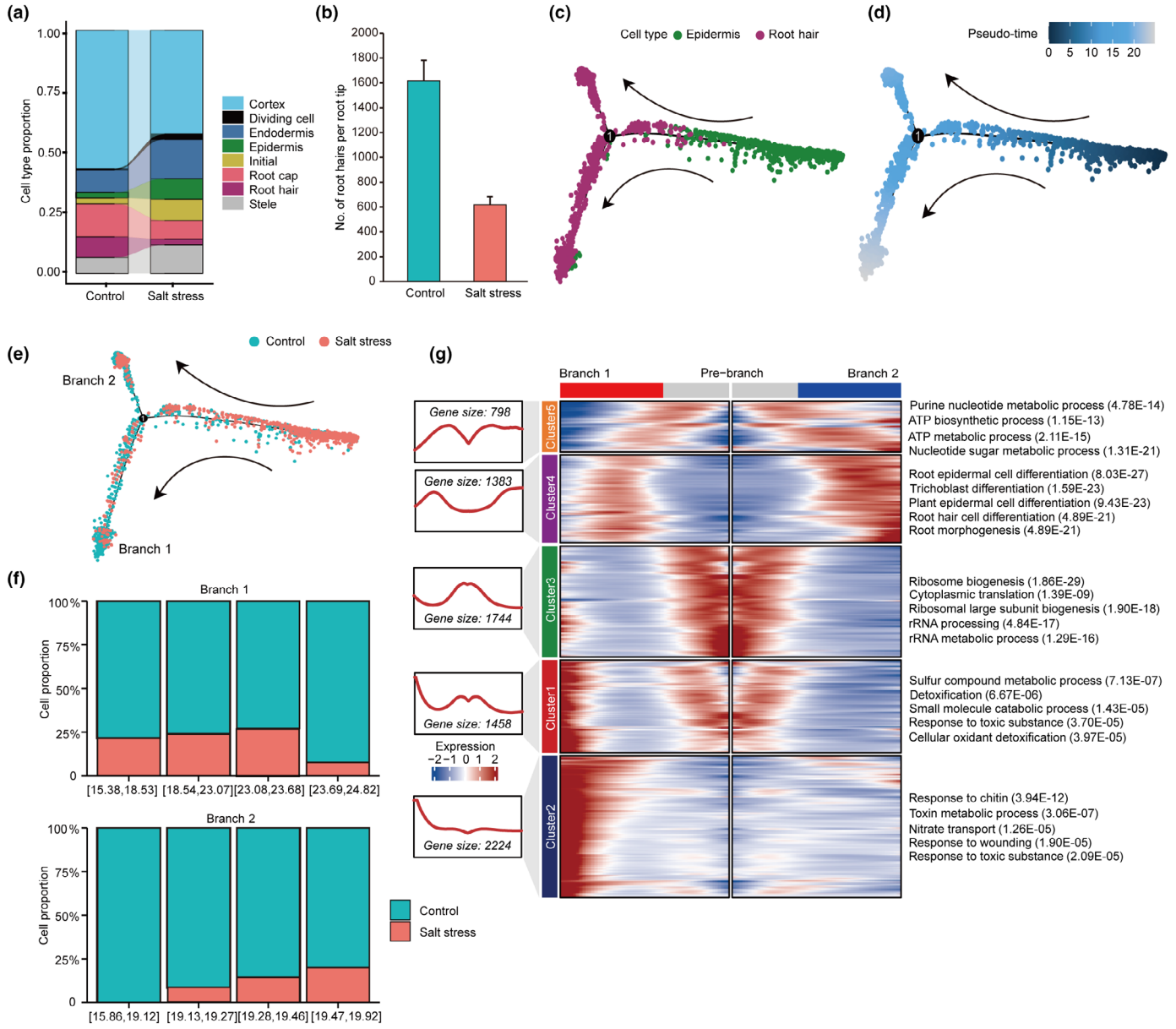

Fig. 3 Salt stress shifts the physiological state of non-heading Chinese cabbage (NHCC) root hair. (a) Cell type proportion in control and salt stress groups. (b) The numbers of root hair cells in 5 mm root tip of control (left) and stress (right) groups respectively. Error bars, mean ± SD, n = 30. (c–e) Pseudo-time trajectory analysis of epidermis and root hair. Cells were colored by cell types (c), pseudo-time (d), and culture conditions (e). (f) Proportional distribution of NHCC control and stress samples in Branch 1 and Branch 2 pseudo-time trajectory, respectively. The proportions were normalized against the total number of cells in each sample. (g) Heatmap showing the expression of regulatory genes on pseudo-time trajectories of epidermis and root hair. The branch point in the middle indicates the beginning of the pseudo-time. The five gene clusters determined by expression patterns were shown on the left, and the Gene Ontology enrichment analyses of each gene cluster were shown on the right. The color bar indicates the relative expression level.

Given that salt stress had a significant effect on root hair phenotypes and response-related genes were significantly reduced in root hair (Fig. 2c,d), we speculated that the physiological states of root hair cells were rewired, from a normal developmental state to a stress-induced state under salt stress. To examine such speculation, we tried to reconstruct the developmental trajectory of root hair cells under normal and salt-stressed conditions. We also performed pseudo-time analysis in each of the identified cell types and found a similar pseudo-time trajectory among cells from both the control and stress groups (Fig. S8). Thus, we highlight the root hair cell state rewiring under salt stress and perform a more detailed analysis. Considering root hair develops from specialized epidermis cells, we included epidermis cells in the pseudo-time analysis to reconstruct root hair development (Figs 3c–e, S9). According to the pseudo-time trajectory, the epidermis was located at the beginning of the trajectory and developed and differentiated into initial root hair along the trajectory. After the bifurcation point, the trajectory gradually diverted into

© 2025 The Author(s).
New Phytologist © 2025 New Phytologist Foundation.

two branches: Branch 1 and Branch 2, representing two different physiological states of root hairs, respectively (Fig. 3c–e).

The stress group contained a higher number of epidermal cells and fewer initial root hairs in the pre-branch (Fig. 3e), leading us to hypothesize that salt stress may have inhibited the transition from epidermis to root hair, which led to the reduction of root hair. To verify our hypothesis, we reconstructed the developmental trajectory of the epidermis (Fig. S10a,b) and analyzed the cell proportions of the control and stress groups at various stages along the pseudo-time trajectory. The proportion of epidermis in the stress group gradually decreased along the pseudo-time developmental trajectory (Fig. S10c). The root hair development process is known to involve four stages: cell fate determination, initiation, elongation, and maturation (Gilroy & Jones, 2000). Since the fate determination and initiation of root hairs were related to the development of the epidermis, we examined the expression of key genes regulating epidermis–root hair development at the single-cell level and found that genes associated with fate determination such as *GL2* (Masucci *et al.*, 1996), *EGL3* (Bernhardt *et al.*, 2003) and *MYB66/ WEREWOLF* (Gilroy & Jones, 2000) were highly expressed in the early and middle stages of the trajectory (Fig. S10d), with no significant changes before and after salt stress(Fig. S10e–g). However, root hair initiation genes including *RHD6* (Jin *et al.*, 2023) and *RSL1* (Feng *et al.*, 2017) were specifically expressed in the late stage of the trajectory (Fig. S10d) and inhibited by salt stress (Fig. S10h,i). Thus, salt stress affected the process of root hair initiation, leading to a reduction in root hair numbers in NHCC.

In addition, cells from the control and salt stress groups were unequally distributed along the two branches. We divided Branch 1 and Branch 2 into four stages along pseudo-time order and calculated the proportion of control and stress root hairs in each stage. In Branch 1, the proportion of root hairs under stress conditions was *c.* 25% in the early stage and gradually decreased in the late stages; in Branch 2, this ratio gradually increased and reached 25% in the later stage, suggesting dramatic but heterogeneous rewiring of the root hair transcriptome under salt stress (Figs 3f, S11).

To uncover key genes and pathways that might mediate the state transition of root hair cells, we identified 7607 DEGs across the pseudo-time order. These genes fell into five clusters with distinct gene expression patterns, representing a transcriptional rewiring program during root hair development (Fig. 3g; Table S9). Genes in Cluster 3 were preferentially expressed in the pre-branch, which consists of epidermal cells. These genes were enriched in GO terms related to cytoplasmic translation. Subsequently, genes in Cluster 4 were highly expressed in Branch 1 and the end of Branch 2, accompanied by the enrichment of genes associated with root hair differentiation (e.g. *RHS11*, *COBL9*) (Li *et al.*, 2022) (Figs 3g, S12; Table S9). These results indicated that cells at the end of Branch 2 were in the stage of root hair differentiation, while cells at the end of Branch 1 were mature cells at the terminal of differentiation. At the end of Branch 1, which contained fewer root hairs in the stress group, genes related to cellular oxidant detoxification, response to wounding, and nitrate transport (e.g. *MPK3*, *AZF3*, *CEK1*; Table S9) were induced (Cluster 1 and Cluster 2). Pseudo-time trajectory reconstruction revealed that there were two physiological states of root hairs with distinct gene expression profiles related to mature (Branch 1) and differentiating (Branch 2) root hairs (Fig. 3g). Taken together, these results suggested that the normal cellular differentiation program was altered under salt stress, with a substantial fraction of root hair cells stacked in an undifferentiated state, preventing the expression of stress-responsive genes.

Evolutionarily conserved root hair gene expression reprogramming in root hair under abiotic stress

To further dissect gene expression changes in root hair under salt stress, we identified primary root hair using pseudo-time results of epidermis and root hair cells and defined the primary root hair as the initiation point of the starting position in the pseudo-time trajectory (Fig. S13a). Pseudo-time trajectory reconstruction showed that root hair cells from the stress group were mainly distributed in the beginning and middle segments of the trajectory, while root hair in the control group was distributed evenly across the whole trajectory (Fig. 4a–c). Subsequently, we divided the developmental trajectory into four stages along pseudo-time order and calculated the proportion of each group in each stage. The proportion of root hairs in the stress group was very high in the early stages of development, *c.* 50%, and gradually decreased in the middle and late stages (Fig. 4d). The phenotypic results showed that the stress group had fewer and shorter root hairs. The epidermis pseudo-time trajectory indicated that salt stress inhibited the initiation of root hairs. Subsequently, we focused on the impact of salt stress on root hair elongation, the post-initiation stage of root hair development. We examined the expression of important bHLH TFs (Yi *et al.*, 2010; Datta *et al.*, 2015) involved in root hair elongation along the root hair pseudo-time trajectory. Interestingly, these genes were expressed in the middle segment of the trajectory (Fig. S14a) and suppressed by salt stress (Fig. S14b–e). These results confirmed that salt stress locked the root hair cells in an immature state by inhibiting their elongation in NHCC.

Our findings that salt stress could shape the physiological states of root hair prompted us to investigate the conservation of such a phenomenon under abiotic stress. To investigate the dynamic expression of conserved genes in root hair under different stressors across species, we compared our NHCC data to snRNA-seq datasets from *Arabidopsis* root tips cultured under normal and osmotic stress conditions (Liu *et al.*, 2024). To ensure the reliability of our cross-species analysis, we used the same parameter set in pseudo-time analysis in *Arabidopsis* and NHCC data. We delineated the developmental trajectory of root hairs in *Arabidopsis*, and the epidermis was defined as the initiation point of the starting position in the pseudo-time trajectory (Fig. S13b). Near the initiation point, the osmotic stress and control groups diverged along the same trajectory, forming two branches at bifurcation point 1: Branch 1 and Branch 2 (Fig. 4e–g). Osmotic stress did not affect Branch 1 cells but inhibited the development of Branch 2 cells (Fig. S15). The proportional distribution of

© 2025 The Author(s).
New Phytologist © 2025 New Phytologist Foundation.

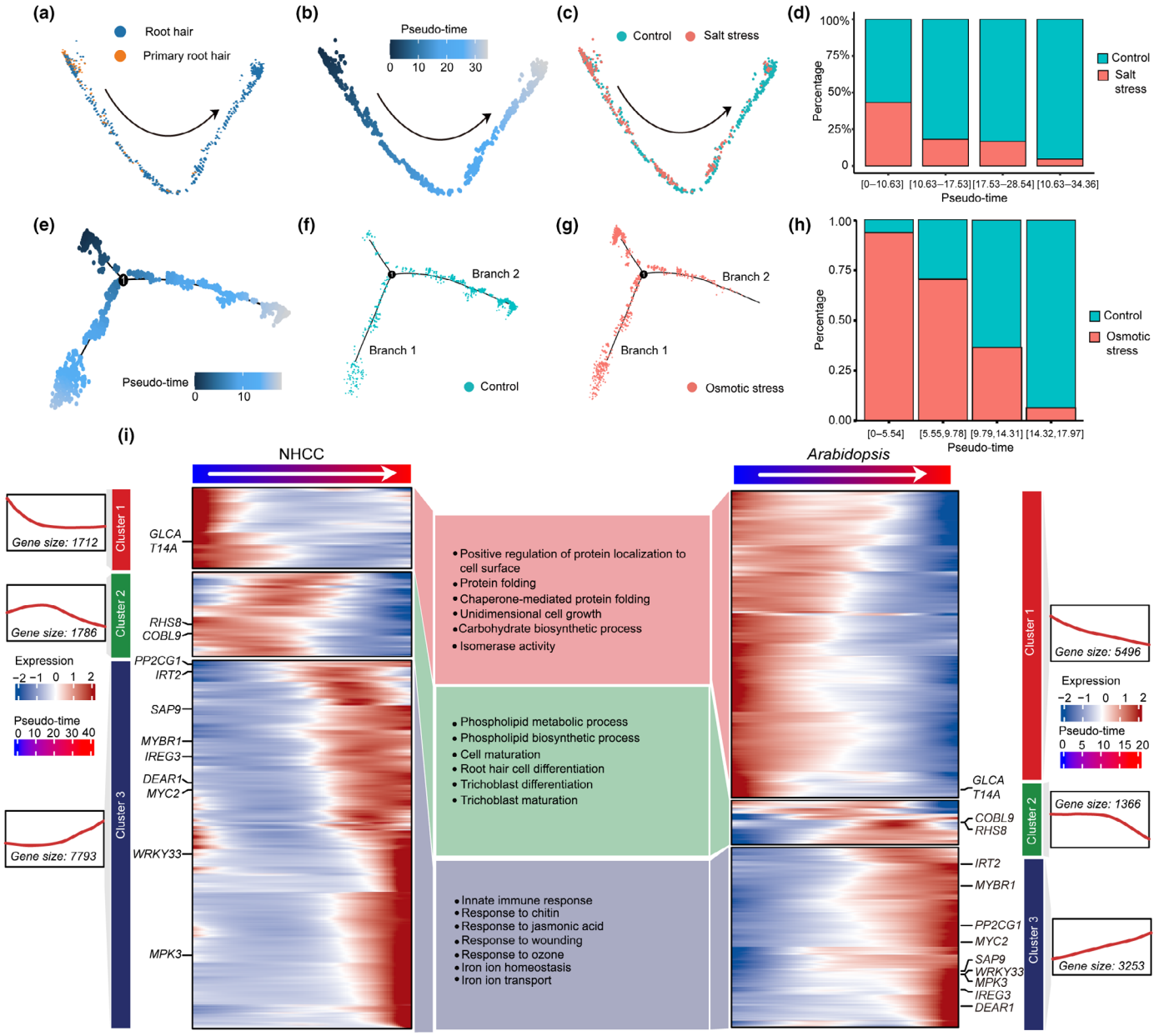

Fig. 4 The converged impacts of different stressors on crucifer root hair were to suppress its development. (a–c) Pseudo-time trajectory analysis of non-heading Chinese cabbage (NHCC) root hair. Cells were colored by cell types (a), pseudo-time (b), and culture conditions (c). (d) Proportional distribution of NHCC control and stress samples in pseudo-time. The proportions were normalized against the total number of cells in each sample. (e–g) Pseudo-time trajectory analysis of *Arabidopsis* root hair. Cells were colored by pseudo-time (e) and culture conditions (f–g). (h) Proportional distribution of *Arabidopsis* control and stress samples in pseudo-time. The proportions were normalized against the total number of cells in each sample. (i) Heatmap showing the expression of regulatory genes on pseudo-time trajectories of NHCC and *Arabidopsis* root hair, respectively. The three gene clusters determined by expression patterns were shown on the two sides, and the common Gene Ontology terms of the two species in each gene cluster were shown in the middle. The color bar indicates the relative expression level. The arrow at the top indicates the direction of the pseudo-time. The annotated orthologs of representative cluster-dependent genes were shown on the two sides of the branch heatmaps.

control and osmotic stress groups at each pseudo-time point was similar to NHCC results (Fig. 4d,h).

To further determine the evolutionary conservation of root hair gene expression changes under abiotic stress, we investigated cross-species co-expressed orthologous genes that exhibited pseudo-time-dependent changes and performed functional enrichment analysis for each expression pattern (Fig. 4i; Table S10). Enrichment analysis of these genes suggested that cell growth, glycoprotein metabolic processes, and carbohydrate biosynthetic processes were highly expressed in both *Arabidopsis* and NHCC cells at the beginning of the curve and were mainly enriched in primary root hair cells. Cluster 2 genes were induced

© 2025 The Author(s).
New Phytologist © 2025 New Phytologist Foundation.

in cells in the middle of the trajectory curve and were involved in cell maturation and trichoblast maturation. Interestingly, the proportion of stress-related cells gradually decreased in the middle stage (Fig. 4d,h), suggesting that the converged impact of different stressors on crucifer root hairs was to inhibit the transition of root hairs from differentiating to mature states.

Cells located at the end of the curves were mature root hairs, genes related to response to jasmonic acid, and response to wounding (Cluster 3, such as *PP2CG1*, *SAP9*, *MYBR1*, *DEAR1*, *MPK3*, *MYC2*, and *WRKY33*) were specifically induced in these cells and implied the environment-responsive role of mature root hair (Fig. 4i). The proportion of mature root hair decreased under various abiotic stresses (Fig. 4d,h), which affected the environmental response function of root hair in both *Arabidopsis* and NHCC. Additionally, ion absorption is one of the important physiological functions of root hair. Genes related to iron transport and iron homeostasis such as *IRT2* (Vert *et al.*, 2001; Vert *et al.*, 2009) and *IREG3* (Schaaf *et al.*, 2006) were also highly expressed in cluster 3, with diminished expression specifically in stressed root hairs in both species (Fig. 4i).

Salt stress inhibits iron uptake by suppressing the development of root hairs

Plants have evolved interrelated regulation networks that enable them to rapidly adapt to environmental changes, and single-cell sequencing allowed us to discover the variances in regulatory networks among distinct cell types. To explore cell type-specific regulatory networks, we associated gene transcription with dynamic accessible chromatin regions (ACRs) at a genome-wide scale. First, we mapped open chromatin regions at the single-cell level in the NHCC root by snATAC-seq. We clustered the cells based on the openness of chromatin identified by snATAC-seq and correlated them with snRNA-seq (Fig. S16). In total, seven clusters were well annotated and correlated. Comparison analysis between snRNA and snATAC results revealed a high correlation for most cell types (Fig. S16g). A lower correlation between transcript levels and ATAC was observed in initial and epidermis cells, suggesting that other factors, such as posttranscriptional regulation, may contribute to the modulation of gene expression.

To systematically reveal cell type-specific regulatory networks, we identified TF-centered regulons by SCENIC, based on co-expression and motif enrichment. In total, we identified 169 TF regulons across eight cell types; the top10 representative TFs for each cell cluster were shown in Fig. 5(a). Heatmapping showed a high correlation between regulon activity and expression of TFs for each cluster (Figs 5b, S17). Given that salt stress had a significant effect on root hair development, we investigated the top 10 representative root hair-specific TF networks (Fig. 5c). Among these, TF *BcRAP2.11* (*LOC103845724*) had a strong correlation with downstream target genes. UMAP visualization revealed that *BcRAP2.11* and its regulon were specifically expressed in root hair and were suppressed under salt stress (Fig. 5d–f). We analyzed BcRAP2.11 downstream target gene expression under control and stress conditions and found that the expression of three target genes was significantly inhibited, whereas others had no obvious changes (Fig. 5g). Among them, *LOC103861180 (BcIRT2)*, the *Arabidopsis IRT2* orthologous gene, was specifically expressed in root hairs (Fig. 5h). We also discovered that the accessible peak number of *LOC103861180* was higher in control root hair than in stressed root hair (Fig. 5i). Interestingly, our pseudo-time analysis also detected that *IRT2* was induced at the mature stage of root hair in both *Arabidopsis* and NHCC (Fig. 4i).

Both the pseudo-time analysis (Fig. 4i) and the cell type-specific regulatory network (Fig. 5c) showed that salt stress inhibited the expression of iron transport-related genes in root hair. The expression of *BcIRT2* was significantly inhibited by salt stress in both *Arabidopsis* and NHCC (Fig. 4i) and regulated by hair-specific TF RAP 2.11. To further explore the contribution of iron deficiency on salt-induced leaf curl and yellowing, we used a turnip yellow mosaic virus-based VIGS system (pTY) and silenced *BcIRT2* in NHCC plants (Yu *et al.*, 2018). At 10 d after treatment with pTY and pTY/BcIRT2, *BcIRT2* expression was examined by RT-qPCR; we could hardly detect *BcIRT2* expression in leaves, and the RT-qPCR result of the root indicated that the transcript level of *BcIRT2* was significantly reduced in plants treated with pTY/BcIRT2 (Fig. S18a). *BcIRT2*-VIGSed plants (#1, #2, and #3) grown under normal conditions showed leaves chlorotic phenotypes similar to those of the pTY under stress (Figs 6a, S18b). To further investigate the role of *BcIRT2* in NHCC, we stained the root tips of normally cultured pTY and *BcIRT2*-VIGSed plants with Perls staining (Roschzttardtz *et al.*, 2009; Vargas & Roschzttardtz, 2023). Perls staining showed that iron content was lower in *BcIRT2*-VIGSed than in pTY-treated plant root tips under normal conditions (Figs 6b, S18c). In addition, iron content was also evaluated in leaves by Perls/DAB staining. We used the DAB intensification method of the Perls staining to augment the sensitivity and precision in detecting iron (Fe) within leaves (Roschzttardtz *et al.*, 2009; Vargas & Roschzttardtz, 2023). Leaf iron content was found to be lower in *BcIRT2*-VIGSed than in pTY plants (Fig. 6c). Our results indicated that *BcIRT2* played an important role in iron ion uptake in NHCC root hairs (Fig. 6a–c). Moreover, *BcIRT2*-VIGSed plants (#4, #5, and #6) showed more curled and yellowed leaves than the pTY under salt stress conditions (Fig. 6a), and the silencing of *BcIRT2* in NHCC led to increased salt sensitivity. Iron content in leaves and root hair was reduced in both pTY and *BcIRT2*-VIGSed plants after salt stress (Fig. 6b, c), and the iron content and root hair length between pTY and *BcIRT2*-VIGSed plants had no significant difference under stress conditions (Figs 6c, S18d).

Then, we focused on the salt stress-related genes in the pTY and *BcIRT2*-VIGSed plants. The following genes, *ABA INSENSITIVE 5(ABI5)*, *ABA INSENSITIVE 2(ABI2)*, *MITOGEN-ACTIVATED PROTEIN KINASE KINASE KINASE 18(MAPKKK18)*, *SnRK2.7*, *ABA-INSENSITIVE PROTEIN KINASE 1(MKKK20)*, and *ABA REPRESSOR1(ABR1)*, which were reported to be key regulators in the salt-responsive pathway, were selected for analysis in pTY and *BcIRT2*-VIGSed plants (Fig. 6d). The expression levels of these genes in the *BcIRT2*-VIGSed root were significantly higher after stress than those in the pTY root, suggesting that silenced *BcIRT2* in NHCC resulted in VIGSed plants being more sensitive to salt

© 2025 The Author(s).
New Phytologist © 2025 New Phytologist Foundation.

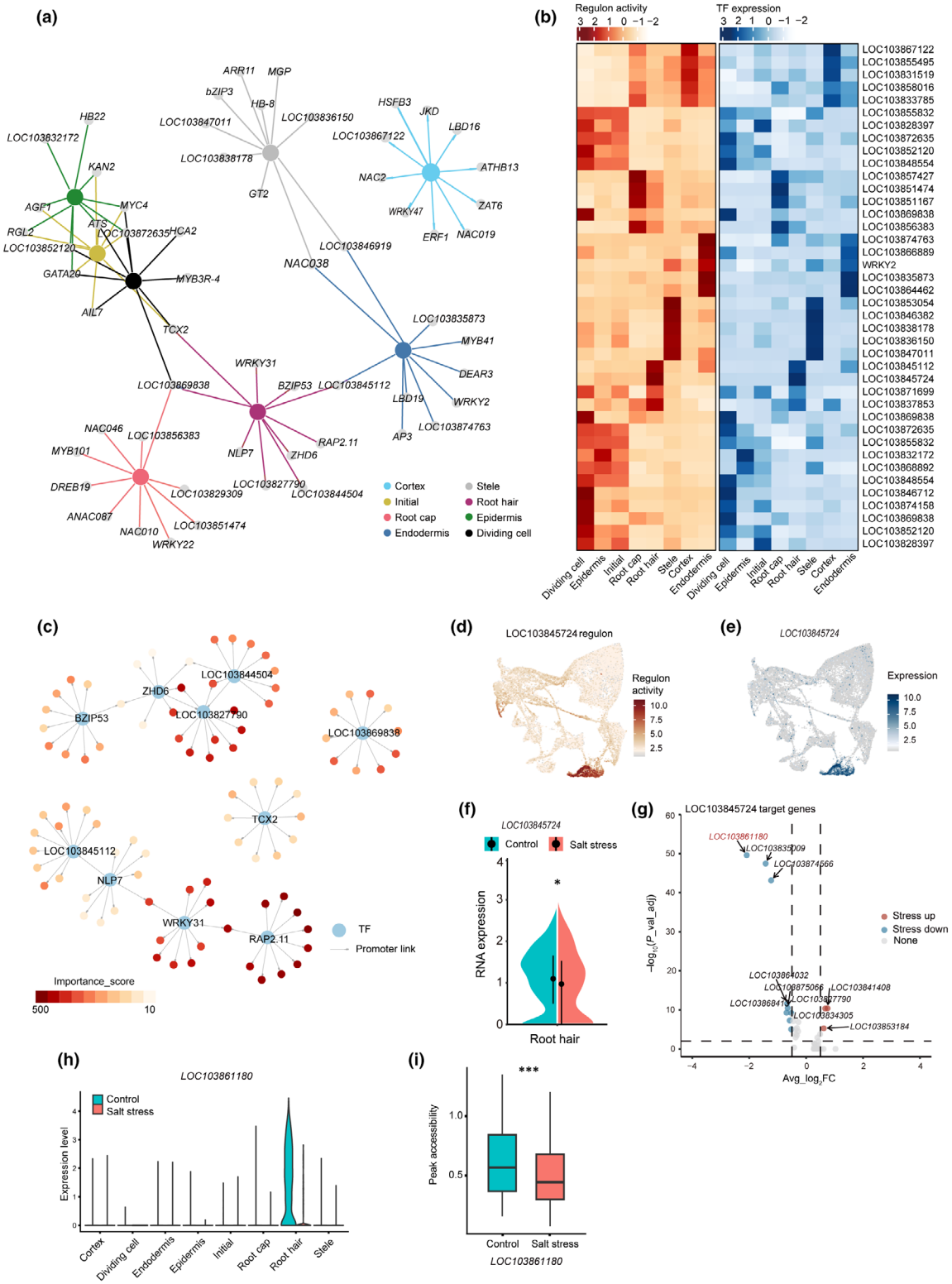

Fig. 5 Cell type-specific regulators and key regulatory networks for non-heading Chinese cabbage (NHCC) root hair. (a) Top 10 representative transcription factor (TF) regulons for each cluster, as identified by SCENIC. (b) Heatmap showing high correlation between regulon activity and expression of TFs for each cluster. (c) Top 10 representative TF regulatory networks of root hairs. (d) Uniform manifold approximation and projection (UMAP) visualization of regulon activity of *LOC10385724*. (e) UMAP visualization of expression of *LOC10385724*. (f) Violin plot of *LOC10385724* expression in different conditions. Error bars, means ± SD; *$P < 0.05$ (Student's *t*-test). (g) Volcano plot showing the expression changes of *LOC10385724* target genes after stress. (h) Violin plot of *LOC103861180* expression in different conditions. (i) Box plot of peak accessibility under different conditions in root hair cells. Center lines show the medians; box limits indicate the 25th and 75th percentiles; whiskers extend 1.5 times the interquartile range from the 25th and 75th percentiles. ***, $P < 0.001$ (Student's *t*-test).

© 2025 The Author(s).
New Phytologist © 2025 New Phytologist Foundation.

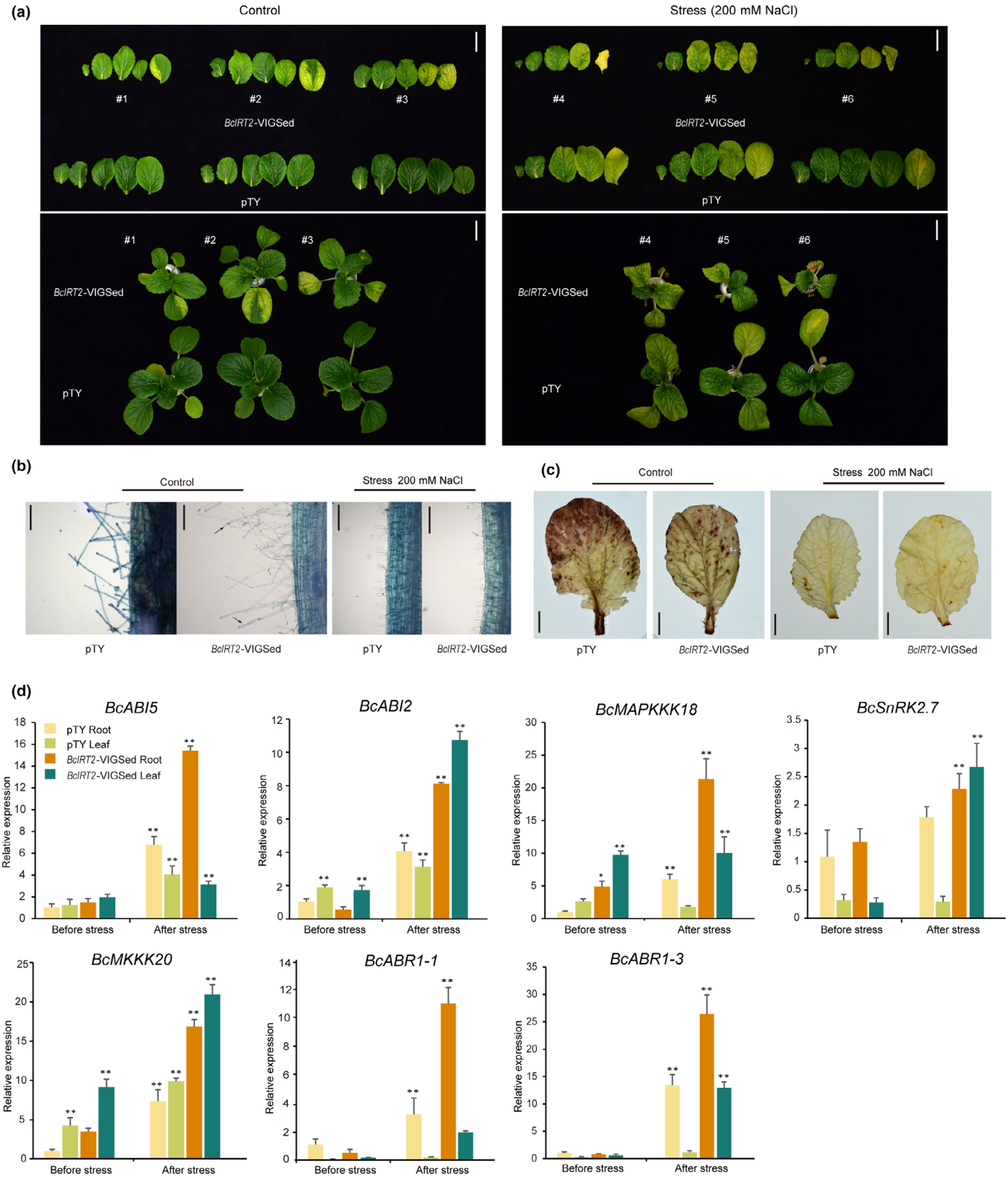

Fig. 6 Salt stress inhibits non-heading Chinese cabbage (NHCC) root hair development leading to decreased iron content. (a) The phenotype of pTY and *BclRT2*-VIGSed plants in control and stress conditions. Photographs of leaves alone showed all true leaves of the corresponding plants in the picture below. Bars, 3 cm. (b) Representative micrographs showing the iron content of root hair from the pTY and *BclRT2*-VIGSed line treated with Perls staining. Arrows indicated low iron content in *BclRT2*-VIGSed plant root hairs. Bars, 200 μm. (c) Perls/DAB staining of NHCC leaves of pTY and *BclRT2*-VIGSed plants under control and stress. Bars, 1 cm. (d) The expression levels of salt-related genes (*BcABI5*, *BcABI2*, *BcMAPKKK18*, *BcSnRK2.7*, *BcMKKK20*, *BcABR1-1*, *BcABR1-2*) in pTY and *BclRT2*-VIGSed plants. All data are averages of three independent experiments, and error bars represent SE. *, $P < 0.05$; **, $P < 0.01$ (Student's *t*-test).

© 2025 The Author(s).
New Phytologist © 2025 New Phytologist Foundation.

stress, consistent with our phenotypic results. The expression of *BcMAPKKK18* was not significantly different after stress in the *BcIRT2-VIGSed* leaf; however, its expression was repressed in the pTY leaf under stress. There were two *ABR1* homologous genes in NHCC; the expression of *BcABR1-1/-2* was induced under stress in the *BcIRT2-VIGSed* leaf, root, and pTY root, while its expression was almost undetectable in pTY leaves. The above results suggested that the signal response mechanism in different tissues under salt stress was discrepant.

Taken together, our results illustrated that salt stress could inhibit root hair development to suppress *BcIRT2* expression (Fig. 4i), leading to the reduction of iron absorption capacity in roots and to abnormal physiological responses such as leaf yellowing in overground plant organs (Fig. 6).

Discussion

A comprehensive understanding of the stress response in plants is essential for precision breeding (Zhu, 2016). Single-cell/nucleus technologies have allowed us to explore transcriptomic and chromatin accessibility changes in a cell type-specific manner, revealing molecular and cellular mechanisms of stress responses (Rich-Griffin *et al.*, 2020). Here, we profiled single-cell transcriptomes of 30 771 nuclei and generated chromatin accessibility landscapes of 24 671 nuclei of NHCC root tips under normal and salt stress conditions. We integrated spatial transcriptomics data and *in situ* hybridization experiments to annotate cell types, identifying novel cell type-specific marker genes and addressing the gap in the lack of marker genes for most cell types of NHCC, contributing to the functional study of NHCC root development.

As the primary tissue responsible for nutrient and water absorption, the root tip interacts with biotic and abiotic microenvironments to regulate overall plant physiology, largely through root hair cells (Gilroy & Jones, 2000). The single-cell transcriptomic atlas allowed us to systematically describe the changes in root tip cells at both cellular and genetic levels during salt stress, providing a more comprehensive understanding of the salt stress response. We observed that salt stress affected the expression of iron uptake-related genes in NHCC using a root hair-specific regulatory network and pseudo-time analysis (Figs 4i, 5c–i). Given the essential role of iron as a micronutrient, acting as a cofactor in a wide variety of pivotal metabolic processes such as the electron transport chain of respiration, photosynthesis, and redox reactions in plants (Spielmann *et al.*, 2023), we further explored the effects of salt stress on iron uptake in NHCC roots. The VIGS assays and Perls staining further demonstrated that salt stress inhibited the development of mature root hairs, significantly affecting their physiological function, especially iron absorption. *BcIRT2*-VIGSed plants had significantly reduced iron content and heightened sensitivity to salt stress (Fig. 6a–c), consistent with our single-cell analysis results. These findings reveal important regulatory relationships between salt stress and iron homeostasis in plants, providing novel perspectives for breeding salt-tolerant NHCC.

Abiotic stresses affect many aspects of plant physiology and cause extensive changes in developmental processes. Some of these changes are nonadaptive responses, reflecting damage caused by stressors, such as detrimental changes in membrane fluidity and protein structure due to heat stress (Zhang *et al.*, 2022). This study's results support that root hair development under salt stress represents a nonadaptive response, losing important physiological functions, such as ion uptake and the ability to respond to environmental factors. This finding was relatively common, as we also observed similar results in the analysis of root hair development under osmotic stress in *Arabidopsis* (Fig. 4i). Our results not only lay a foundation for further studies on NHCC root development but also suggest that future abiotic stress breeding programs should consider the plasticity of root hair morphology.

As the first single-cell multi-omic analysis of the NHCC root tip, this research has limitations. First, the root tip was highly complex, and we observed strong heterogeneity even within cell types, such as root hair cells. Despite the overall decrease in root hair density and length under salt stress, we illustrated an increase in root hair length and density in the meristem (Fig. S7). The limited number of cells in root hair restricted in-depth analysis of this heterogeneity. A study in *Brassica napus* found that 100 mM NaCl imposed for 55 d after germination leads to an increased density and number of root hairs in first-order and second-order lateral roots (Arif *et al.*, 2019), indicating that the response pattern of mature plant roots to salt stress was different from the seedling stage. Future research, including a larger number of cells with spatial and developmental information, will more comprehensively elucidate this heterogeneity. Second, the regulatory analysis in this study was performed on material from the same genetic background, and future population-level gene regulatory analysis in genetically diverse materials will generate insights into genetic variants that regulate key gene expression in NHCC.

Acknowledgements

We sincerely thank the China National GenBank (CNGB) for the support they provided. This work was supported by grants from the National Natural Science Foundation of China (32330096; 32202505; U24A20417), Hebei Natural Science Foundation (C2023204308; C2024204246), Hebei S&T Bureau (2023HBQZYCSB009), and Science Foundation of Ministry of Education of China (MoE, 902/1123401).

Competing interests

None declared.

Author contributions

JZ, WM and XL conceptualized the project. QL, JK, ZL, QW, HL, HH and XZ performed the experiments. LD, QL, JK and KW analyzed the data. QL, LD, YH, WM and QC prepared the manuscript. All authors read and approved the final manuscript.

© 2025 The Author(s).
New Phytologist © 2025 New Phytologist Foundation.

QL, JK, LD and ZL contributed equally to this work (co-first authors).

ORCID

Lin Du https://orcid.org/0009-0006-7669-5728
Yiguo Hong https://orcid.org/0000-0002-3352-9686
Jingmin Kang https://orcid.org/0009-0006-5901-5268
Qing Liu https://orcid.org/0009-0008-0830-622X
Xin Liu https://orcid.org/0000-0003-3256-2940
Wei Ma https://orcid.org/0000-0001-5716-6106
Jianjun Zhao https://orcid.org/0000-0001-7364-1974

Data availability

The NHCC raw data that support the findings of this study have been deposited into the CNGB Sequence Archive (CNSA) (Guo *et al.*, 2020) of China National GeneBank DataBase (CNGBdb) (Chen *et al.*, 2020) with accession no. CNP0005053 (snATAC-seq data and snRNA-seq data): https://db.cngb.org/search/project/CNP0005053/. The Stereo-seq data is available under accession no. STT0000066: https://db.cngb.org/stomics/project/STT0000066/spatialGeneExpression.

The *Arabidopsis* raw data that support the findings of this study have been deposited in the NCBI GEO with the accession no. GSE235495.

References

Ahanger MA, Aziz U, Alsahli AA, Alyemeni MN, Ahmad P. 2019. Influence of exogenous salicylic acid and nitric oxide on growth, photosynthesis, and ascorbate-glutathione cycle in salt stressed *Vigna angularis*. *Biomolecules* **10**: 42.

Aibar S, González-Blas CB, Moerman T, Huynh-Thu VA, Imrichova H, Hulselmans G, Rambow F, Marine JC, Geurts P, Aerts J *et al.* 2017. SCENIC: single-cell regulatory network inference and clustering. *Nature Methods* **14**: 1083–1086.

Arif MR, Islam MT, Robin AHK. 2019. Salinity stress alters root morphology and root hair traits in *Brassica napus*. *Plants* **8**: 192.

Bawa G, Liu Z, Yu X, Tran LP, Sun X. 2024. Introducing single cell stereo-sequencing technology to transform the plant transcriptome landscape. *Trends in Plant Science* **29**: 249–265.

Bernhardt C, Lee MM, Gonzalez A, Zhang F, Lloyd A, Schiefelbein J. 2003. The bHLH genes *GLABRA3* (*GL3*) and *ENHANCER OF GLABRA3* (*EGL3*) specify epidermal cell fate in the *Arabidopsis* root. *Development* **130**: 6431–6439.

Cai X, Chang L, Zhang T, Chen H, Zhang L, Lin R, Liang J, Wu J, Freeling M, Wang X. 2021. Impacts of allopolyploidization and structural variation on intraspecific diversification in *Brassica rapa*. *Genome Biology* **22**: 166.

Chen A, Liao S, Cheng M, Ma K, Wu L, Lai Y, Qiu X, Yang J, Xu J, Hao S *et al.* 2022. Spatiotemporal transcriptomic atlas of mouse organogenesis using DNA nanoball-patterned arrays. *Cell* **185**: 1777–1792.

Chen FZ, You LJ, Yang F, Wang LN, Guo XQ, Gao F, Hua C, Tan C, Fang L, Shan RQ *et al.* 2020. CNGBdb: China National GeneBank database. *Hereditas* **42**: 799–809.

Datta S, Prescott H, Dolan L. 2015. Intensity of a pulse of RSL4 transcription factor synthesis determines *Arabidopsis* root hair cell size. *Nature Plants* **28**: 15138.

Denyer T, Ma X, Klesen S, Scacchi E, Nieselt K, Timmermans MCP. 2019. Spatiotemporal developmental trajectories in the *Arabidopsis* root revealed using high-throughput single-cell RNA sequencing. *Developmental Cell* **48**: 840–852.

Ding Y, Gao W, Qin Y, Li X, Zhang Z, Lai W, Yang Y, Guo K, Li P, Zhou S *et al.* 2023. Single-cell RNA landscape of the special fiber initiation process in Bombax ceiba. *Plant Communications* **4**: 100554.

Dinneny JR, Long TA, Wang JY, Jung JW, Mace D, Pointer S, Barron C, Brady SM, Schiefelbein J, Benfey PN. 2008. Cell identity mediates the response of *Arabidopsis* roots to abiotic stress. *Science* **320**: 942–945.

Farmer A, Thibivilliers S, Ryu KH, Schiefelbein J, Libault M. 2021. Single-nucleus RNA and ATAC sequencing reveals the impact of chromatin accessibility on gene expression in *Arabidopsis* roots at the single-cell level. *Molecular Plant* **14**: 372–383.

Feng Y, Xu P, Li B, Li P, Wen X, An F, Gong Y, Xin Y, Zhu Z, Wang Y *et al.* 2017. Ethylene promotes root hair growth through coordinated EIN3/EIL1 and RHD6/RSL1 activity in *Arabidopsis*. *Proceedings of the National Academy of Sciences, USA* **114**: 13834–13839.

Filgueiras CC, Martins AD, Pereira RV, Willett DS. 2019. The ecology of salicylic acid signaling: primary, secondary and tertiary effects with applications in agriculture. *International Journal of Molecular Sciences* **20**: 5851.

Geng Y, Wu R, Wee CW, Xie F, Wei X, Chan PM, Tham C, Duan L, Dinneny JR. 2013. A spatio-temporal understanding of growth regulation during the salt stress response in *Arabidopsis*. *Plant Cell* **25**: 2132–2154.

Gilroy S, Jones DL. 2000. Through form to function: root hair development and nutrient uptake. *Trends in Plant Science* **5**: 56–60.

Granja JM, Corces MR, Pierce SE, Bagdatli ST, Choudhry H, Chang HY, Greenleaf WJ. 2021. ArchR is a scalable software package for integrative single-cell chromatin accessibility analysis. *Nature Genetics* **53**: 403–411.

Guo X, Chen F, Gao F, Li L, Liu K, You L, Hua C, Yang F, Liu W, Peng C *et al.* 2020. CNSA: a data repository for archiving omics data. *Database* **2020**: baaa055.

Hao Y, Hao S, Andersen-Nissen E, Mauck WM 3rd, Zheng S, Butler A, Lee MJ, Wilk AJ, Darby C, Zager M *et al.* 2021. Integrated analysis of multimodal single-cell data. *Cell* **184**: 3573–3587.

Huang MD, Wu WL. 2007. Overexpression of TMAC2, a novel negative regulator of abscisic acid and salinity responses, has pleiotropic effects in *Arabidopsis thaliana*. *Plant Molecular Biology* **63**: 557–569.

Jin D, Li S, Li Z, Yang L, Han X, Hu Y, Jiang Y. 2023. *Arabidopsis* ABRE-binding factors modulate salinity-induced inhibition of root hair growth by interacting with and suppressing *RHD6*. *Plant Science* **332**: 111728.

Karaba A, Dixit S, Greco R, Aharoni A, Trijatmiko KR, Marsch-Martinez N, Krishnan A, Nataraja KN, Udayakumar M, Pereira A. 2007. Improvement of water use efficiency in rice by expression of *HARDY*, an *Arabidopsis* drought and salt tolerance gene. *Proceedings of the National Academy of Sciences, USA* **104**: 15270–15275.

Kumar N, Mishra B, Athar M, Mukhtar S. 2021. Inference of gene regulatory network from single-cell transcriptomic data using pySCENIC. *Methods in Molecular Biology* **2328**: 171–182.

Lareau CA, Duarte FM, Chew JG, Kartha VK, Burkett ZD, Kohlway AS, Pokholok D, Aryee MJ, Steemers FJ, Lebofsky R *et al.* 2019. Droplet-based combinatorial indexing for massive-scale single-cell chromatin accessibility. *Nature Biotechnology* **37**: 916–924.

Lei Y, Cheng M, Li Z, Zhuang Z, Wu L, Sun Y, Han L, Huang Z, Wang Y, Wang Z *et al.* 2022. Spatially resolved gene regulatory and disease-related vulnerability map of the adult Macaque cortex. *Nature Communications* **13**: 6747.

Li H, Durbin R. 2010. Fast and accurate long-read alignment with Burrows-Wheeler transform. *Bioinformatics* **26**: 589–595.

Li Y, Liu GF, Ma LM, Liu TK, Zhang CW, Xiao D, Zheng HK, Chen F, Hou XL. 2020. A chromosome-level reference genome of non-heading Chinese cabbage [*Brassica campestris* (syn. *Brassica rapa*) ssp. *chinensis*]. *Horticulture Research* **7**: 212.

Li Y, Ma H, Wu Y, Ma Y, Yang J, Li Y, Yue D, Zhang R, Kong J, Lindsey K *et al.* 2024. Single-cell transcriptome atlas and regulatory dynamics in developing cotton anthers. *Advanced Science* **11**: e2304017.

Li Z, Zhou T, Sun P, Chen X, Gong L, Sun P, Ge S, Liang YK. 2022. *COBL9* and *COBL7* synergistically regulate root hair tip growth via controlling apical cellulose deposition. *Biochemical and Biophysical Research Communications* **596**: 6–13.

Liang Z, Brown RC, Fletcher JC, Opsahl-Sorteberg HG. 2015. Calpain-mediated positional information directs cell wall orientation to sustain plant

© 2025 The Author(s).
New Phytologist © 2025 New Phytologist Foundation.

stem cell activity, growth and development. *Plant & Cell Physiology* **56**: 1855–1866.

Libault M, Brechenmacher L, Cheng J, Xu D, Stacey G. 2010. Root hair systems biology. *Trends in Plant Science* **15**: 641–650.

Liu C, Wu T, Fan F, Liu Y, Wu L, Junkin M, Wang Z, Yu Y, Wang W, Wei W *et al.* 2019. A portable and cost-effective microfluidic system for massively parallel single cell transcriptome profiling. *BioRxiv*. doi: 10.1101/818450.

Liu Q, Ma W, Chen R, Li ST, Wang Q, Wei C, Hong Y, Sun HX, Cheng Q, Zhao J *et al.* 2024. Multiome in the same cell reveals the impact of osmotic stress on *Arabidopsis* root tip development at single-cell level. *Advanced Science* **11**: e2308384.

Ma W, Zhang P, Zhao J, Hong Y. 2023. Chinese cabbage: an emerging model for functional genomics in leafy vegetable crops. *Trends in Plant Science* **28**: 515–518.

Marand AP, Chen Z, Gallavotti A, Schmitz RJ. 2021. A *cis*-regulatory atlas in maize at single-cell resolution. *Cell* **184**: 3041–3055.e21.

Martin J, Wang Z. 2011. Next-generation transcriptome assembly. *Nature Reviews Genetics* **12**: 671–682.

Masucci JD, Rerie WG, Foreman DR, Zhang M, Galway ME, Marks MD, Schiefelbein JW. 1996. The homeobox gene GLABRA2 is required for position-dependent cell differentiation in the root epidermis of *Arabidopsis thaliana*. *Development* **122**: 1253–1260.

Mo Y, Jiao Y. 2022. Advances and applications of single-cell omics technologies in plant research. *The Plant Journal* **110**: 1551–1563.

Qiu X, Hill A, Packer J, Lin D, Ma YA, Trapnell C. 2017. Single-cell mRNA quantification and differential analysis with census. *Nature Methods* **14**: 309–315.

Qu J, Yang F, Zhu T, Wang Y, Fang W, Ding Y, Zhao X, Qi X, Xie Q, Chen M *et al.* 2022. A reference single-cell regulomic and transcriptomic map of cynomolgus monkeys. *Nature Communications* **13**: 4069.

Ramachandran P, Augstein F, Mazumdar S, Nguyen TV, Minina EA, Melnyk CW, Carlsbecker A. 2021. Abscisic acid signaling activates distinct VND transcription factors to promote xylem differentiation in *Arabidopsis*. *Current Biology* **31**: 3153–3161.

Ren Y, Wang W, He J, Zhang L, Wei Y, Yang M. 2020. Nitric oxide alleviates salt stress in seed germination and early seedling growth of pakchoi (*Brassica chinensis* L.) by enhancing physiological and biochemical parameters. *Ecotoxicology and Environmental Safety* **187**: 109785.

Rich-Griffin C, Stechemesser A, Finch J, Lucas E, Ott S, Schäfer P. 2020. Single-cell transcriptomics: a high-resolution avenue for plant functional genomics. *Trends in Plant Science* **25**: 186–197.

Roschzttardtz H, Conéjéro G, Curie C, Mari S. 2009. Identification of the endodermal vacuole as the iron storage compartment in the *Arabidopsis* embryo. *Plant Physiology* **151**: 1329–1338.

Schaaf G, Honsbein A, Meda AR, Kirchner S, Wipf D, von Wirén N. 2006. *AtIREG2* encodes a tonoplast transport protein involved in iron-dependent nickel detoxification in *Arabidopsis thaliana* roots. *The Journal of Biological Chemistry* **281**: 25532–25540.

Shahan R, Hsu CW, Nolan TM, Cole BJ, Taylor IW, Greenstreet L, Zhang S, Afanassiev A, Vlot AHC, Schiebinger G *et al.* 2022. A single-cell *Arabidopsis* root atlas reveals developmental trajectories in wild-type and cell identity mutants. *Developmental Cell* **57**: 543–560.

Shaw R, Tian X, Xu J. 2021. Single-cell transcriptome analysis in plants: advances and challenges. *Molecular Plant* **14**: 115–126.

Shi Q, Liu S, Kristiansen K, Liu L. 2022. The FASTQ+ format and PISA. *Bioinformatics* **38**: 4639–4642.

Spielmann J, Fanara S, Cotelle V, Vert G. 2023. Multilayered regulation of iron homeostasis in *Arabidopsis*. *Frontiers in Plant Science* **14**: 1250588.

Sun X, Feng D, Liu M, Qin R, Li Y, Lu Y, Zhang X, Wang Y, Shen S, Ma W *et al.* 2022. Single-cell transcriptome reveals dominant subgenome expression and transcriptional response to heat stress in Chinese cabbage. *Genome Biology* **23**: 262.

Traag VA, Waltman L, van Eck NJ. 2019. From Louvain to Leiden: guaranteeing well-connected communities. *Scientific Reports* **9**: 5233.

Vargas J, Roschzttardtz H. 2023. Perls/DAB staining to examine iron distribution in *Arabidopsis* embryos. *Methods in Molecular Biology* **2665**: 173–176.

Vert G, Barberon M, Zelazny E, Séguéla M, Briat JF, Curie C. 2009. *Arabidopsis* IRT2 cooperates with the high-affinity iron uptake system to maintain iron homeostasis in root epidermal cells. *Planta* **229**: 1171–1179.

Vert G, Briat JF, Curie C. 2001. *Arabidopsis IRT2* gene encodes a root-periphery iron transporter. *The Plant Journal* **26**: 181–189.

Waadt R, Seller CA, Hsu PK, Takahashi Y, Munemasa S, Schroeder JI. 2022. Plant hormone regulation of abiotic stress responses. *Nature Reviews. Molecular Cell Biology* **23**: 680–694.

Wang H, Li Z, Ren H, Zhang C, Xiao D, Li Y, Hou X, Liu T. 2022. Regulatory interaction of BcWRKY33A and BcHSFA4A promotes salt tolerance in non-heading Chinese cabbage [*Brassica campestris* (syn. *Brassica rapa*) ssp. *chinensis*]. *Horticulture Research* **9**: uhac113.

Wang X, Bi S, Wang L, Li H, Gao BA, Huang S, Qu X, Cheng J, Wang S, Liu C *et al.* 2020. GLABRA2 regulates actin bundling protein VILLIN1 in root hair growth in response to osmotic stress. *Plant Physiology* **184**: 176–193.

Wang Y, Zhang W, Li K, Sun F, Han C, Wang Y, Li X. 2008. Salt-induced plasticity of root hair development is caused by ion disequilibrium in *Arabidopsis thaliana*. *Journal of Plant Research* **121**: 87–96.

Wendrich JR, Yang B, Vandamme N, Verstaen K, Smet W, Van de Velde C, Minne M, Wybouw B, Mor E, Arents HE *et al.* 2020. Vascular transcription factors guide plant epidermal responses to limiting phosphate conditions. *Science* **370**: eaay4970.

Wolf FA, Angerer P, Theis FJ. 2018. SCANPY: large-scale single-cell gene expression data analysis. *Genome Biology* **19**: 15.

Wong GR, Mazumdar P, Lau SE, Harikrishna JA. 2018. Ectopic expression of a Musa acuminata root hair defective 3 (MaRHD3) in *Arabidopsis* enhances drought tolerance. *Journal of Plant Physiology* **231**: 219–233.

Xia K, Sun HX, Li J, Li J, Zhao Y, Chen L, Qin C, Chen R, Chen Z, Liu G *et al.* 2022. The single-cell stereo-seq reveals region-specific cell subtypes and transcriptome profiling in *Arabidopsis* leaves. *Developmental Cell* **57**: 1299–1310.

Yang Y, Guo Y. 2018. Elucidating the molecular mechanisms mediating plant salt-stress responses. *New Phytologist* **217**: 523–539.

Yi K, Menand B, Bell E, Dolan L. 2010. A basic helix-loop-helix transcription factor controls cell growth and size in root hairs. *Nature Genetics* **42**: 264–267.

Yu J, Yang XD, Wang Q, Gao LW, Yang Y, Xiao D, Liu TK, Li Y, Hou XL, Zhang CW. 2018. Efficient virus-induced gene silencing in Brassica rapa using a turnip yellow mosaic virus vector. *Biologia Plantarum* **62**: 826–834.

Yu Z, Duan X, Luo L, Dai S, Ding Z, Xia G. 2020. How plant hormones mediate salt stress responses. *Trends in Plant Science* **25**: 1117–1130.

Zhang F, Wu Y, Tian W. 2019. A novel approach to remove the batch effect of single-cell data. *Cell Discovery* **5**: 46.

Zhang L, Cai X, Wu J, Liu M, Grob S, Cheng F, Liang J, Cai C, Liu Z, Liu B *et al.* 2018. Improved *Brassica rapa* reference genome by single-molecule sequencing and chromosome conformation capture technologies. *Horticulture Research* **5**: 50.

Zhang L, He C, Lai Y, Wang Y, Kang L, Liu A, Lan C, Su H, Gao Y, Li Z *et al.* 2023. Asymmetric gene expression and cell-type-specific regulatory networks in the root of bread wheat revealed by single-cell multiomics analysis. *Genome Biology* **24**: 65.

Zhang M, Smith JA, Harberd NP, Jiang C. 2016. The regulatory roles of ethylene and reactive oxygen species (ROS) in plant salt stress responses. *Plant Molecular Biology* **91**: 651–659.

Zhang TQ, Chen Y, Liu Y, Lin WH, Wang JW. 2021. Single-cell transcriptome atlas and chromatin accessibility landscape reveal differentiation trajectories in the rice root. *Nature Communications* **12**: 2053.

Zhang X, Ma W, Liu M, Li X, Li J, Lu Y, Li G, Zhang S, Feng D, Wang Y *et al.* 2022. OCTOPUS regulates BIN2 to control leaf curvature in Chinese cabbage. *Proceedings of the National Academy of Sciences, USA* **119**: e2208978119.

Zhang Y, Liu T, Meyer CA, Eeckhoute J, Johnson DS, Bernstein BE, Nusbaum C, Myers RM, Brown M, Li W *et al.* 2008. Model-based analysis of ChIP-Seq (MACS). *Genome Biology* **9**: R137.

Zhao C, Zhang H, Song C, Zhu JK, Shabala S. 2020. Mechanisms of plant responses and adaptation to soil salinity. *Innovations* **1**: 100017.

Zhao Y, Hu Y, Dai M, Huang L, Zhou DX. 2009. The WUSCHEL-related homeobox gene *WOX11* is required to activate shoot-borne crown root development in rice. *Plant Cell* **21**: 736–748.

Zhu JK. 2016. Abiotic stress signaling and responses in plants. *Cell* **167**: 313–324.

© 2025 The Author(s).
New Phytologist © 2025 New Phytologist Foundation.

Supporting Information

Additional Supporting Information may be found online in the Supporting Information section at the end of the article.

Fig. S1 UMAP visualization of two biological replicates and two or three technical replicates in the control and stress group.

Fig. S2 Expression of marker genes of each cell type in the control and stress group.

Fig. S3 The 6-d-old root tips were revealed by aniline blue staining of longitudinal sections and cross sections.

Fig. S4 Expression of cortex marker genes (orthologous of *Arabidopsis*) of each cell type.

Fig. S5 Estimation of the Stereo-seq data quality.

Fig. S6 RNA *in situ* hybridization detection of cell type-specific genes.

Fig. S7 Statistical analysis of root hair phenotypes.

Fig. S8 Pseudo-time trajectory analysis of cortex, dividing cell, endodermis, initial, root cap, and stele.

Fig. S9 Expression of cell type marker genes on the pseudo-time trajectory.

Fig. S10 Pseudo-time trajectory analysis of NHCC epidermis.

Fig. S11 Proportional distribution of NHCC stress samples in Branch 1 and Branch 2 pseudo-time trajectory.

Fig. S12 The expression patterns of root hair genes BcRHS11 and BcCOBL9 in the trajectory plot and UMAP plot.

Fig. S13 Confirmation of the developmental trajectory initial sites.

Fig. S14 Salt stress inhibited the elongation of root hair in NHCC.

Fig. S15 Proportional distribution of *Arabidopsis* control and stress samples in Branch 1 and Branch 2 pseudo-time trajectory.

Fig. S16 Mapping the chromatin accessibility information revealed by snATAC-seq into the cell clusters classified by snRNA-seq.

Fig. S17 Heatmap showing high correlation between regulon activity and TF expression for each cluster.

Fig. S18 Identification and phenotype observation of BcIRT2-VIGSed plants.

Table S1 The primers used in RNA *in situ* hybridization.

Table S2 Quantitative real-time PCR (RT-qPCR) primers.

Table S3 The original data report summary for snRNA-seq, snATAC-seq, and Stereo-seq.

Table S4 Well-studied marker genes in *Arabidopsis thaliana*.

Table S5 GO enrichment of stress-up and stress-down genes for each cluster.

Table S6 Well-studied genes related to ethylene biosynthesis, ABA transport and biosynthesis, and SA biosynthesis in *Arabidopsis thaliana*.

Table S7 Salt stress related genes in *Arabidopsis*.

Table S8 Number of nuclei captured by snRNA-seq for each cell type.

Table S9 GO enrichment analysis of five gene clusters in Fig. 3g pseudo-time trajectories.

Table S10 GO enrichment analysis of three gene clusters in Fig. 4i pseudo-time trajectories.

Please note: Wiley is not responsible for the content or functionality of any Supporting Information supplied by the authors. Any queries (other than missing material) should be directed to the *New Phytologist* Central Office.

Disclaimer: The New Phytologist Foundation remains neutral with regard to jurisdictional claims in maps and in any institutional affiliations.

© 2025 The Author(s).
New Phytologist © 2025 New Phytologist Foundation.